UvA-DARE (Digital Academic Repository)

Water content and wind acceleration in the envelope around the oxygen-rich AGB star IK Tauri as seen by Herschel/HIFI

Decin, L.; Justtanont, K.; De Beck, E.; Lombaert, R.; de Koter, A.; Waters, L.B.F.M.; Marston, A.P.; Teyssier, D.; Schöier, F.L.; Bujarrabal, V.; Alcolea, J.; Cernicharo, J.; Dominik, C.; Melnick, G.; Menten, K.; Neufeld, D.A.; Olofsson, H.; Planesas, P.; Schmidt, M.; Szczerba, R.; de Graauw, T.; Helmich, F.; Roelfsema, P.; Dieleman, P.; Morris, P.; Gallego, J.D.; Díez-González, M.C.; Caux, E.

Link to publication

Herschel/HIFI: first science highlights

Astronomy & Astrophysics

Special feature

L$_{\text{ETTER}}$ $_{\text{TO THE}}$ E$_{\text{DITOR}}$

Water content and wind acceleration in the envelope around the oxygen-rich AGB star IK Tauri as seen by *Herschel*/HIFI[⋆],[⋆⋆]

L. Decin[1,2], K. Justtanont[3], E. De Beck[1], R. Lombaert[1], A. de Koter[2,4], L. B. F. M. Waters[2], A. P. Marston[5], D. Teyssier[5], F. L. Schöier[13], V. Bujarrabal[6], J. Alcolea[7], J. Cernicharo[8], C. Dominik[2,22], G. Melnick[9], K. Menten[10], D. A. Neufeld[11], H. Olofsson[12,13], P. Planesas[7,14], M. Schmidt[15], R. Szczerba[15], T. de Graauw[16], F. Helmich[17], P. Roelfsema[17], P. Dieleman[17], P. Morris[18], J. D. Gallego[19], M. C. Díez-González[19], and E. Caux[20,21]

(Affiliations are available on page 5 of the online edition)

ABSTRACT

During their asymptotic giant branch evolution, low-mass stars lose a significant fraction of their mass through an intense wind, enriching the interstellar medium with products of nucleosynthesis. We observed the nearby oxygen-rich asymptotic giant branch star IK Tau using the high-resolution HIFI spectrometer onboard *Herschel*. We report on the first detection of $H_2^{16}O$ and the rarer isotopologues $H_2^{17}O$ and $H_2^{18}O$ in both the ortho and para states. We deduce a total water content (relative to molecular hydrogen) of 6.6×10^{-5}, and an ortho-to-para ratio of 3:1. These results are consistent with the formation of H_2O in thermodynamical chemical equilibrium at photospheric temperatures, and does not require pulsationally induced non-equilibrium chemistry, vaporization of icy bodies or grain surface reactions. High-excitation lines of ^{12}CO, ^{13}CO, ^{28}SiO, ^{29}SiO, ^{30}SiO, HCN, and SO have also been detected. From the observed line widths, the acceleration region in the inner wind zone can be characterized, and we show that the wind acceleration is slower than hitherto anticipated.

Key words. line: profiles – radiative transfer – instrumentation: spectrographs – stars: AGB and post-AGB – circumstellar matter – submillimeter: stars

1. Introduction

IK Tau, also known as NML Tau, is an extremely red, oxygen-rich, Mira-type variable, with a period of about 470 days (Wing & Lockwood 1973). Its dust-driven wind produces a cool circumstellar envelope (CSE), which fosters a rich gas-phase chemistry (e.g., Duari et al. 1999). IK Tau is relatively nearby, at a distance of ~265 pc (Hale et al. 1997). Estimates of its mass-loss rates range from 3.8×10^{-6} (Neri et al. 1998) to 3×10^{-5} $M_\odot$/yr (González Delgado et al. 2003). IK Tau's proximity and relatively high mass-loss rate facilitate the observation of molecular emission lines. Currently, a dozen different molecules and some of their isotopologs have been discovered in IK Tau, including CO, HCN, SiO, SiS, SO, SO$_2$, and NaCl (e.g. Milam et al. 2007; Decin et al. 2010).

In this Letter, we report on the detection of thermal emission of water (H_2O) in the envelope around IK Tau. The main isotopolog ($H_2^{16}O$) as well as the rarer isotopologs ($H_2^{17}O$ and $H_2^{18}O$) are detected for both the ortho- and para-states. We also present observations of high-excitation rotational transitions of ^{12}CO, ^{13}CO, ^{28}SiO, ^{29}SiO, ^{30}SiO, HCN, and SO and demonstrate that the observed line widths characterize the acceleration region in the inner wind zone.

2. Observations and data reduction

The HIFI instrument (de Graauw et al. 2010) onboard the *Herschel* satellite (Pilbratt et al. 2010) offers the possibility to observe molecular fingerprints in the frequency ranges of 480–1150 GHz and 1410–1910 GHz at a spectral resolution up to 125 kHz. Single-point observations towards IK Tau were carried out with the *Herschel*/HIFI instrument in the dual beam switch (DBS) mode with a 3′ chop throw. The observation strategy and data-reduction are discussed in Appendix A and in Bujarrabal et al. (2010).

3. Results

In the 13 single-point observations obtained so far, covering a frequency range of 92.8 GHz in total, 31 molecular emission lines have been detected belonging to ^{12}CO, ^{13}CO, $H_2^{16}O$, $H_2^{17}O$, $H_2^{18}O$, ^{28}SiO, ^{29}SiO, ^{30}SiO, HCN, SO, and NH$_3$ (see Table A.2 in the Appendix). The detection of NH$_3$ is described in Menten et al. (2010).

For the first time, different excitation lines of water are discovered for the two nuclear spin isomers, ortho- and para-$H_2^{16}O$, as well as for the rare isotopologs $H_2^{17}O$ and $H_2^{18}O$ (see Fig. 1). The observations of these transitions provide information about the total water content, the ortho-to-para ratio, and the isotopic ratios $H_2^{16}O/H_2^{17}O$ and $H_2^{16}O/H_2^{18}O$ (see Sect. 3.1).

High-excitation rotational transitions are observed for different molecules (see Fig. 2). From the observed line widths, which range between 11 and 19 km s^{-1}, it is immediately clear that the HIFI observations offer us a strong diagnostic to trace the wind acceleration zone in the inner envelope (see Sect. 3.2). Moreover, the high-excitation ^{12}CO $J = 10$–9 and $J = 16$–15 lines, complemented with ground-based observations of ^{12}CO for $J = 1$–0 to $J = 7$–6, can be used as temperature indicator for the envelope as close as ~20 $R_\star$ (see Sect. 3.2).
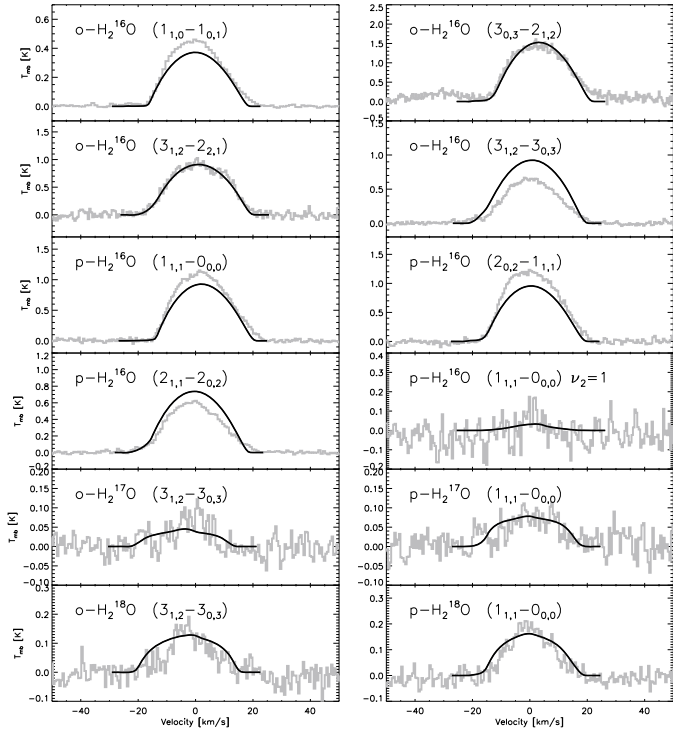

Fig. 1. HIFI observations of water lines (gray) compared to their line profile predictions (black). *Row 1–2:* ortho-$H_2^{16}O$, *row 3–4:* para-$H_2^{16}O$, *row 5:* ortho and para-$H_2^{17}O$, and *row 6:* ortho and para-$H_2^{18}O$.

3.1. Water in IK Tau's envelope

Water content: We observed both ortho and para-water lines for different isotopologs in IK Tau (Fig. 1). Using the analytical formula from Groenewegen (1994), we calculated a photodissociation radius of 2.8×10^{16} cm or 1870 $R_\star$, while the theoretical models by Willacy & Millar (1997) predict a value around 1600 $R_\star$. Assuming the same photodissociation radius for all isotopologs and isomers, we deduced (see Appendix B) a water-abundance [ortho-$H_2^{16}O/H_2$] = 5×10^{-5} and an ortho-to-para water ratio (OPR) of 3:1. Taking the uncertainty in the photodissociation radius into account, the estimated uncertainty in the water abundance is a factor 2 for the assumed envelope structure (see Sect. 3.2).

The total (ortho+para) $H_2^{16}O$ abundance for IK Tau derived in this Letter, relative to the total hydrogen content and assuming that all hydrogen is in the form of molecular hydrogen, is $[H_2^{16}O/H_{tot}] = 3.3 \times 10^{-5}$, slightly lower than the photospheric thermodynamic equilibrium (TE) prediction of 7×10^{-5} for an evolved star with a C/O ratio of 0.75 (Cherchneff 2006). The theoretical TE value for the total water abundance is, however, very dependent on the exact value of the C/O ratio, which is unknown for IK Tau. Cherchneff (2006) predicts a higher inner wind abundance of 3.5×10^{-4} around 5 $R_\star$ in the case of pulsationally induced non-equilibrium chemistry. The upper limit implied by the cosmic abundances of carbon and oxygen is no more than 1×10^{-3}, assuming that all carbon is locked in CO and the remaining oxygen goes into H_2O (Anders & Grevesse 1989). Vaporization of icy bodies (Justtanont et al. 2005) or grain surface reactions via Fischer-Tropsch catalysis (Willacy 2004) will also result in a higher water abundance. Considering the agreement between the derived and the TE abundance, the effects of the other processes seem negligible for IK Tau.

On the basis of ISO-LWS data, Maercker et al. (2008) derived for IK Tau an ortho-$H_2^{16}O$ abundance (relative to H_2) of 3.5×10^{-4}, significantly higher than the value we derived. Both studies used an almost equal photodissociation radius. However, Maercker et al. (2008) only included the ground-state for the excitation analysis. As shown by Decin et al. (2010), neglecting the first vibrational state of the bending mode, $\nu_2 = 1$, leads to an underprediction of the HIFI transitions here presented. Since the ISO data used in the study of Maercker et al. are saturated, the integrated intensity is insensitive to the exact value of the abundance, which will result in an overprediction of the H_2O-abundance. We also note that the H_2O line profile predictions are quite sensitive to the exact value of the kinetic temperature and the dust radiation field (and wavelength-dependent absorption efficiencies) (Decin et al. 2010), which in part might also explain the difference between the value we derive [ortho-$H_2^{16}O/H_2$] = 5×10^{-5} and the value of Maercker et al. (2008) [ortho-$H_2^{16}O/H_2$]=3.5×10^{-4}. A comparison with the ISO-LWS data will be presented in Decin et al. (in prep.).

For the oxygen-rich Mira W Hya, Zubko & Elitzur (2000) derived an OPR value of 1:1.3 and Barlow et al. (1996) reported a value of 1:1. However, Barlow et al. noted that their derived value is quite uncertain, due to the high opacities in the water lines used. Justtanont et al. (2010) derived an OPR of 2.1:1 for the S-type AGB χ Cyg. Our study here is the first time that the OPR value in an oxygen-rich Mira is determined from a combination of emission lines of $H_2^{16}O$, $H_2^{17}O$, and $H_2^{18}O$. The advantage of using the rarer isotopologs is that the opacity of the lines is lower, making the line intensities more sensitive to the OPR value. The observed para-water lines are consistent with an OPR value of 3:1 (±0.4). The lowest energy level of para-H_2O is ~34 K below that of ortho-H_2O. When water forms in the gas phase via exothermic reactions the energy released is much greater than this energy difference and the OPR reflects the high-temperature (~50 K) thermodynamic 3:1 ratio of the statistical weights between the species. The derived OPR value of 3:1 confirms that water in IK Tau is formed in warm and dense regions of the envelope where the chemistry is in thermodynamical equilibrium.

Isotope ratios: Assuming the same photodissociation radius as for the main isotopolog, the isotopic ratios we derive for IK Tau are $H_2^{16}O/H_2^{17}O$ = 600 (±150) and $H_2^{16}O/H_2^{18}O$ = 200 (±50), hence well below the solar values ($^{16}O/^{17}O \sim 2632$ and $^{16}O/^{18}O \sim 499$; Asplund et al. 2009). Interpreting the derived isotopic ratios in terms of nucleosynthesis and subsequent dredge-ups or extra mixing processes is quite complex (e.g. Harris et al. 1985, 1987; Karakas et al. 2010). In stars that are sufficiently massive to undergo CNO-cycle hydrogen burning, the low initial ^{17}O abundance (assumed to be solar) is enhanced. When helium burning begins inside the hydrogen-burning shell, ^{17}O is expected to be completely destroyed in the region where maximum hydrogen burning occurs. The isotope ^{18}O, on the other hand, is expected to be destroyed during hydrogen burning, so that it virtually disappears from the hydrogen-burning zone and from the hydrogen-exhausted CNO equilibrium zone within it. When helium burning starts, the ^{18}O abundance might slightly increase. A succession of convective mixings brings to the surface material that is affected by these nuclear transformations. Calculations by Harris et al. (1985) show that in every star that becomes a red giant star ($M \gtrsim 0.8\ M_\odot$), the initial $^{16}O/^{17}O$ ratio decreases to ~440 during the first dredge-up, while the $^{16}O/^{18}O$ slightly increases. The second dredge-up occurs at the end of core helium burning only for the most massive intermediate-mass stars ($M \gtrsim 4.5\ M_\odot$). The estimated
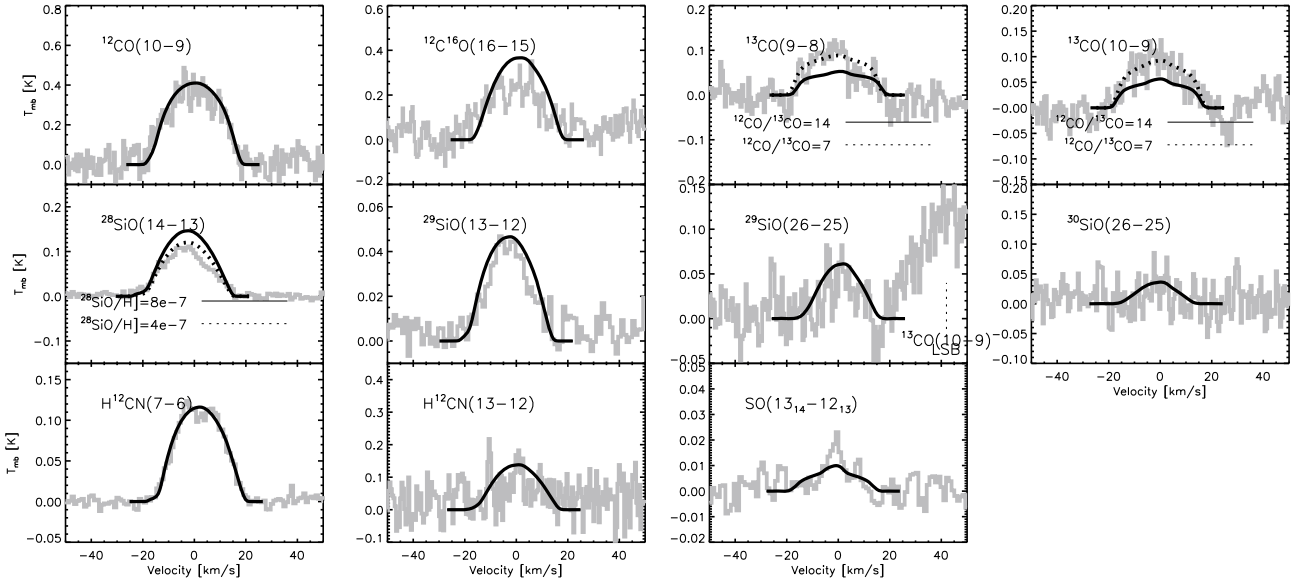
Fig. 2. HIFI observations of line transitions of several molecules (gray) compared to their line profile predictions (black). Full black lines refer to line predictions using the molecular abundance stratifications as determined by Decin et al. (2010), dotted black lines show the model predictions for the refined fractional abundances as determined in this Letter (see Appendix B).

$^{16}O/^{17}O$ ratio ranges between 150 and 500, while the $^{16}O/^{18}O$ ratio slightly increases. The third dredge-up occurs in the subsequent helium shell-burning phase for stars $\geq 2\ M_{\odot}$, and is expected to yield isotopic ratios of $^{16}O/^{17}O \leq 200$. If hot bottom burning occurs (for stars above 3–4 $M_{\odot}$), the $^{16}O/^{17}O$ ratio will be of the order of 20–50. That the $^{16}O/^{17}O$ ratio is around 600, implies that the first but no subsequent dredge-ups occurred and constrains the initial mass of IK Tau to be within 1–2 $M_{\odot}$. Alternatively, if the star is more massive than 2 $M_{\odot}$ and the third dredge-up has occurred (but has not turned the star into a carbon-rich star), transferred material from a post-third dredge-up envelope must have had a $^{16}O/^{17}O$ ratio ≤ 200. This implies that in stars with $^{16}O/^{17}O \sim 600$ the transferred material has been heavily diluted by material from the star's own envelope with much higher $^{16}O/^{17}O$ ratios. From Fig. 5 of Harris et al. (1987), it is estimated that IK Tau has a low s-process neutron exposure, $\tau_0 \leq 0.1$, implying a low absolute enhancement of the s-process elements and only a few third dredge-up events, consistent with IK Tau still being an oxygen-rich AGB star.

Hitherto, the lower than solar $^{16}O/^{18}O$ ratios cannot be explained by any stellar evolution model in the literature. However, IK Tau is not the only Galactic star with a low $^{16}O/^{18}O$ ratio (see Fig. 3 in Karakas et al. 2010); some barium stars analyzed by Harris et al. (1985) also have a low $^{16}O/^{18}O$ value. It is anticipated that the observations of other evolved stars in the framework of the HIFISTARS programme (P.I. V. Bujarrabal) will add new information to this discussion.

3.2. Thermodynamical structure of the envelope

Being a simple diatomic molecule with a well understood energy diagram, CO has been successfully used to study the structure of the CSEs around evolved stars (e.g., Schöier et al. 2002; Decin et al. 2006). Different transitions can be used to investigate different regions of the envelope, probing the density, the temperature, and the velocity of the CSE. Decin et al. (2010) used the $^{12}CO\ J = 1$–0 to $J = 7$–6 lines to determine the thermophysical structure of the CSE of IK Tau beyond $\sim 100\ R_{\star}$, based on a non-local thermodynamic equilibrium (non-LTE) radiative transfer analysis of the available transitions. In the first instance,

the kinetic temperature and velocity structure of the envelope were calculated by solving the equations of motion of gas and dust and the energy balance simultaneously. To get insight into the structure in the inner wind region, the HCN $J = 3$–2 and $J = 4$–3 transitions were used, since observational evidence exists that HCN is formed close to the star ($\lesssim 3.85''$, Marvel 2005). The Gaussian HCN line profiles indeed point toward line formation partially in the inner wind where the stellar wind has not yet reached its full terminal velocity (Bujarrabal & Alcolea 1991). The results of Decin et al. (2010) infer a wind acceleration that is lower than derived from solving the momentum equation.

3.2.1. Temperature structure

Adopting the thermodynamic structure derived in Decin et al. (2010) (and reproduced in Fig. B.1 of the Appendix), the theoretical line profiles for the $^{12}CO\ J = 10$–9 and $J = 16$–15 are calculated (see Fig. 2) using the non-LTE radiative transfer code GASTRoNOoM (Decin et al. 2006, 2010). The $^{12}CO\ J = 10$–9 line is very well reproduced, while the $J = 16$–15 line exhibits slightly larger deviations. The latter most likely reflects the very difficult calibration of this frequency setting (for which standing waves heavily perturbed the baseline, see Bujarrabal et al. 2010). This result is consistent with the temperature structure in the region between 20 and 100 $R_{\star}$ derived by Decin et al. (2010).

3.2.2. Velocity structure

To constrain the wind acceleration in the CSE, all molecular emission lines as shown in Figs. 1–2 were modelled (see Appendix B). The line formation region of each molecular line was estimated by considering the range of projected radii where $I_{\nu_0}(p)\,p\,dp$, with I_{ν_0} the intensity at the line center and p the impact parameter, exceeds half of its maximum value (see Fig. 3). We note that the radial extent of the line formation region is almost insensitive to the exact value of the velocity structure. Optical depths effects can strongly affect the observed line widths, and detailed radiative transfer modelling (as presented in this Letter) is required to determine the underlying velocity structure. Most of the observed lines have line widths in excess of 17 km s^{-1}. However, a few lines are considerably narrower,
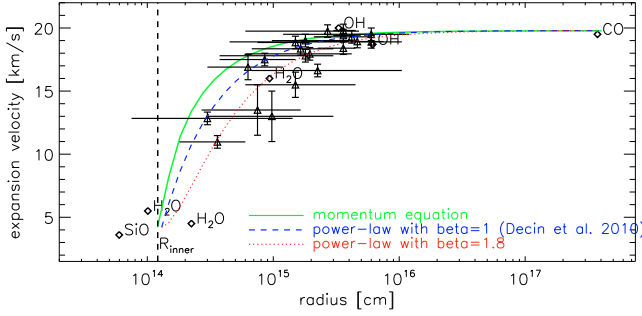
Fig. 3. Velocity profile of IK Tau. Velocity data are obtained from mapping of maser emission: SiO (Boboltz & Diamond 2005), H$_2$O (Bains et al. 2003), and OH (Bowers et al. 1989). The CO expansion velocity derived from ground-based CO $J = 1$–0 data is also indicated (Decin et al. 2010). The triangles show the place in the envelope where the line formation is highest for the HIFI data presented in Figs. 1–2, i.e., where $I_{\nu_0}(p) \, p^2$ is at its maximum. The horizontal bars show the minimum and maximum radial distance for the line formation of each individual transition. The vertical bars show the uncertainty on the observed line widths. The expansion velocity deduced from solving the momentum equation is shown by the full green line. The dashed blue line represents a power law (Eq. (1)) with $\beta = 1$ (as used for the modelling in Appendix B). For comparison, an even smoother expansion velocity structure with $\beta = 1.8$ is shown with the red dotted line. The vertical dashed black line indicates the dust condensation radius R_{inner}. The velocity at R_{inner} is assumed to be equal to the local sound velocity.

and their line formation regions are located in that part of the envelope where the wind has not yet reached its terminal velocity (19 km s^{-1}). Although the line formation regions are quite broad, we find the first observational evidence that the wind acceleration is slower than implied by the momentum equation, corroborating the results of Decin et al. (2010). Using the classical β-parametrization (e.g., Lamers & Cassinelli 1999) to simulate the velocity structure,

$$v(r) \simeq v_0 + (v_\infty - v_0)\left(1 - \frac{R_\star}{r}\right)^\beta , \qquad (1)$$

where v_0 is the velocity at the dust condensation radius and v_∞ is the terminal velocity, we find that $1 \leq \beta \leq 2$. The theoretical line predictions shown in this Letter are computed for $\beta = 1$. The momentum equation, in contrast, matches a much steeper velocity profile with $\beta = 0.6$. We note that the velocity structure derived by Justtanont et al. (2010) for χ Cyg is compliant with a β-value of 0.9. As discussed by Decin et al. (2010), there are several possible causes for a less steep velocity structure. We summarize that a slower wind velocity may be caused by incomplete momentum coupling, dust emission being slightly optically thick to the stellar radiation, the fact that not all dust species are formed at the same time and at the same radial distance, and/or that some dust species are inefficient as wind drivers.

4. Conclusions

Using the HIFI spectrometer onboard *Herschel*, we have observed the evolved oxygen-rich Mira star, IK Tau, in 31 molecular emission lines. For the first time, several lines of ortho and para H$_2^{16}$O, and the rarer isotoplogs H$_2^{17}$O and H$_2^{18}$O have been detected. We have deduced a total water content (relative to H$_2$) of 6.6×10^{-5}, and an ortho-to-para ratio of 3:1. The measured thermal emission from water therefore points toward TE

chemistry, as opposed to pulsationally induced non-equilibrium chemistry, grain surface reactions, or evaporation of icy bodies. For the isotopic ratios, we find subsolar values H$_2^{16}$O/H$_2^{17}$O = 600 and H$_2^{16}$O/H$_2^{18}$O = 200.

The high-excitation lines of ^{12}CO, ^{13}CO, ^{28}SiO, ^{29}SiO, ^{30}SiO, HCN, and SO indicate that the wind acceleration is slower than hitherto anticipated from solving the momentum equation. These results show the great capability of HIFI to study the complex thermodynamical and chemical envelopes of evolved stars in tremendous detail.

References

Anders, E., & Grevesse, N. 1989, Geochim. Cosmochim. Acta, 53, 197
Asplund, M., Grevesse, N., Sauval, A. J., & Scott, P. 2009, ARA&A, 47, 481
Bains, I., Cohen, R. J., Louridas, A., et al. 2003, MNRAS, 342, 8
Barlow, M. J., Nguyen-Q-Rieu, Truong-Bach, et al. 1996, A&A, 315, L241
Boboltz, D. A., & Diamond, P. J. 2005, ApJ, 625, 978
Bowers, P. F., Johnston, K. J., & de Vegt, C. 1989, ApJ, 340, 479
Bujarrabal, V., & Alcolea, J. 1991, A&A, 251, 536
Bujarrabal, V. Alcolea, J., Soria-Ruiz, R., et al. 2010, A&A, 521, L3
Cherchneff, I. 2006, A&A, 456, 1001
Decin, L., Hony, S., de Koter, A., et al. 2006, A&A, 456, 549
Decin, L., De Beck, E., Brunken, S., et al. 2010, A&A, 516, A69
de Graauw, Th., Helmich, F. P., Philips, T., et al. 2010, A&A, 518, L6
Duari, D., Cherchneff, I., & Willacy, K. 1999, A&A, 341, L47
Faure, A., Crimier, N., Ceccarelli, C., et al. 2007, A&A, 472, 1029
González Delgado, D., Olofsson, H., Kerschbaum, F., et al. 2003, A&A, 411, 123
Groenewegen, M. A. T. 1994, A&A, 290, 531
Hale, D. D. S., Bester, M., Danchi, W. C., et al. 1997, ApJ, 490, 407
Harris, M. J., Lambert, D. L., & Smith, V. V. 1985, ApJ, 292, 620
Harris, M. J., Lambert, D. L., Hinkle, K. H., et al. 1987, ApJ, 316, 294
Justtanont, K., Bergman, P., Larsson, B., et al. 2005, A&A, 439, 627
Justtanont, K., Decin, L., Schöier, F. L., et al. 2010, A&A, 521, L6
Karakas, A. I., Campbell, S. W., & Stancliffe, R. J. 2010, ApJ, 713, 374
Lamers, H. J. G. L. M., & Cassinelli, J. P. 1999, Introduction to Stellar Winds, ed. H. J. G. L. M. Lamers, & J. P. Cassinelli
Maercker, M., Schöier, F. L., Olofsson, H., et al. 2008, A&A, 479, 779
Mamon, G. A., Glassgold, A. E., & Huggins, P. J. 1988, ApJ, 328, 797
Marvel, K. B. 2005, AJ, 130, 261
Menten, K., Wyrowski, F., Alcolea, J., et al. 2010, A&A, 521, L7
Milam, S. N., Apponi, A. J., Woolf, N. J., & Ziurys, L. M. 2007, ApJ, 668, L131
Neri, R., Kahane, C., Lucas, R., Bujarrabal, V., & Loup, C. 1998, A&AS, 130, 1
Pilbratt, G. L., Riedinger, J. R., Passvogel, T., et al. 2010, A&A, 518, L1
Rothman, L. S., Gordon, I. E., Barbe, A., et al. 2009, JQSRT, 110, 533
Schöier, F. L., Ryde, N., & Olofsson, H. 2002, A&A, 391, 577
Willacy, K. 2004, ApJ, 600, L87
Willacy, K., & Millar, T. J. 1997, A&A, 324, 237
Wing, R. F., & Lockwood, G. W. 1973, ApJ, 184, 873
Zubko, V., & Elitzur, M. 2000, ApJ, 544, L137

1 Instituut voor Sterrenkunde, Katholieke Universiteit Leuven, Celestijnenlaan 200D, 3001 Leuven, Belgium
e-mail: Leen.Decin@ster.kuleuven.be
2 Sterrenkundig Instituut Anton Pannekoek, University of Amsterdam, Science Park 904, 1098 Amsterdam, The Netherlands
3 Onsala Space observatory, Chalmers University of Technology, Dept. Radio & Spece Science, 439 92 Onsala, Sweden
4 Astronomical Institute, Utrecht University, Princetonplein 5, 3584 CC Utrecht, The Netherlands
5 European Space Astronomy Centre, ESA, PO Box 78, 28691 Villanueva de la Cañada, Madrid, Spain
6 Observatorio Astronómico Nacional. Ap 112, 28803 Alcalá de Henares, Spain
e-mail: v.bujarrabal@oan.es
7 Observatorio Astronómico Nacional (IGN), Alfonso XII No 3, 28014 Madrid, Spain
8 Laboratory of Molecular Astrophysics, CAB, INTA-CSIC, Ctra de Torrejón a Ajalvir, km 4, 28850 Torrejón de Ardoz, Madrid, Spain
9 Harvard-Smithsonian Center for Astrophysics, Cambridge, MA 02138, USA
10 Max-Planck-Institut für Radioastronomie, Auf dem Hügel 69, 53121 Bonn, Germany
11 John Hopkins University, Baltimore, MD 21218, USA
12 Department of Astronomy, AlbaNova University Center, Stockholm University, 10691 Stockholm, Sweden
13 Onsala Space Observatory, Dept. of Radio and Space Science, Chalmers University of Technology, 43992 Onsala, Sweden
14 Joint ALMA Observatory, El Golf 40, Las Condes, Santiago, Chile
15 N. Copernicus Astronomical Center, Rabiańska 8, 87-100 Toruń, Poland
16 Atacama Large Millimeter/Submillimeter Array, Joint ALMA Office, Santiago, Chile
17 SRON Netherlands Institute for Space Research, Landleven 12, 9747 AD Groningen, The Netherlands
18 Infrared Processing and Analysis Center, California Institute of Technology, MS 100-22, Pasadena, CA 91125, USA
19 Observatorio Astronómico Nacional (IGN), Centro Astronómico de Yebes, Apartado 148. 19080 Guadalajara, Spain
20 Centre d'Étude Spatiale des Rayonnements, Université de Toulouse [UPS], 31062 Toulouse Cedex 9, France
21 CNRS/INSU, UMR 5187, 9 avenue du Colonel Roche, 31028 Toulouse Cedex 4, France
22 Department of Astrophysics/IMAPP, Radboud University Nijmegen, PO Box 9010, 6500 GL Nijmegen, The Netherlands

Appendix A: Details about the observation strategy and data reduction

Table A.1. LO frequencies ν_{LO}, main beam efficiencies η_{MB} according to Eq. (A.1), velocity resolution Δv (for 0.5 MHz frequency resolution), and operational days (OD) when observations were carried out.

ν_{LO} (GHz)	η_{MB}	Δv (km s⁻¹)	OD
564.476	0.69	0.27	292
614.763	0.68	0.24	292
758.772	0.68	0.20	297
975.087	0.67	0.15	293
995.481	0.67	0.15	293
1102.757	0.67	0.14	294
1106.735	0.67	0.14	294
1157.495	0.67	0.13	296
1200.717	0.66	0.12	296
1713.596	0.64	0.09	298
1757.417	0.63	0.09	298
1838.039	0.63	0.08	298
1864.539	0.63	0.08	298

The regular DBS mode was used for bands 1 up to 5, while FastDBS was applied to bands 6 and 7 to achieve higher stability with respect to electrical standing waves. Two orthogonal polarizations were measured simultaneously. The double-sideband (DSB, Helmich et al., in prep.) observations ensure an instantaneous 8 GHz and 5.2 GHz frequency coverage by the wide band spectrometer (WBS) for respectively bands 1 up to 5, and bands 6 and 7. The spectral resolution is 0.5 MHz. Care was taken in choosing local oscillator (LO) frequencies such that no strong lines from the two sidebands would blend, and that at the same time a maximum number of molecular lines would be covered.

The data were processed with the standard HIFI pipeline using HIPE, and non-stitched Level-2 data were exported using the HiClass tool available in HIPE. Further processing, i.e. blanking spurious signals, baseline removal, stitching of the spectrometer subbands, and averaging, was performed in CLASS. When the quality of the spectra measured in both horizontal and vertical polarization was good, these were averaged to lower the rms noise. This approach is justified since polarisation is not a concern for the presented molecular-line analysis. In all cases, we assumed a side-band gain ratio of one.

All data presented in this Letter were converted from the antenna-temperature (T_A^*) scale to the main-beam temperature (T_{MB}) scale according to $T_{MB} = T_A^*/\eta_{MB}$, with values of the main-beam efficiency η_{MB} (Table A.1) calculated for the LO frequency ν_{LO}, according to

$$\eta_{MB} = \eta_B \times \exp\left(-\left(\frac{\nu_{LO}/GHz}{6 \times 10^3}\right)^2\right) \times \eta_F, \qquad (A.1)$$

with $\eta_B = 0.72$ and $\eta_F = 0.96$ being the beam efficiency in the 0 Hz frequency limit and the forward efficiency, respectively. The absolute calibration accuracy ranges from 10% for the lowest frequency lines up to 30% for the high frequency (>1 THz) lines.

Appendix B: Radiative transfer modelling

The molecular emission lines shown in Figs. 1–2, were modelled using the non-LTE radiative transfer code GASTRoNOoM (Decin et al. 2006). Last updates to the code and a discussion of

Table A.2. Observation summary.

Molecule	Transition	Freq. [GHz]	I [K km s⁻¹]	Noise [K]	Comments
o-H₂¹⁶O	$1_{1,0}-1_{0,1}$	556.936	10.22	0.005	
o-H₂¹⁶O	$5_{3,2}-4_{4,1}$	620.701	14.89	0.005	maser
o-H₂¹⁶O	$3_{1,2}-3_{0,3}$	1097.365	14.44	0.036	
o-H₂¹⁶O	$3_{1,2}-2_{2,1}$	1153.127	22.60	0.062	
o-H₂¹⁶O	$3_{0,3}-2_{1,2}$	1716.770	30.89	0.104	
o-H₂¹⁶O	$5_{3,2}-5_{2,3}$	1867.749	3.45	0.118	standing waves
o-H₂¹⁶O	$3_{2,1}-3_{1,2}$	1162.912	13.70	0.062	
p-H₂¹⁶O	$2_{1,1}-2_{0,2}$	752.033	13.71	0.015	
p-H₂¹⁶O	$5_{2,4}-4_{3,1}$	970.315	19.34	0.026	maser
p-H₂¹⁶O	$2_{0,2}-1_{1,1}$	987.927	27.85	0.030	
p-H₂¹⁶O	$1_{1,1}-0_{0,0}$	1113.343	25.10	0.028	
p-H₂¹⁶O	$1_{1,1}-0_{0,0}\ \nu_2=1$	1205.798	0.59	0.070	tentative, see Fig. 1
p-H₂¹⁶O	$4_{2,2}-4_{1,3}$	1207.639	8.21	0.070	maser
p-H₂¹⁶O	$5_{3,3}-6_{0,6}$	1716.953	1.03	0.104	standing waves
o-H₂¹⁷O	$3_{1,2}-3_{0,3}$	1096.414	1.20	0.036	
p-H₂¹⁷O	$1_{1,1}-0_{0,0}$	1107.167	1.50	0.036	
o-H₂¹⁸O	$3_{1,2}-3_{0,3}$	1095.627	2.52	0.036	
p-H₂¹⁸O	$1_{1,1}-0_{0,0}$	1101.699	3.57	0.028	
¹²C¹⁶O	10–9	1151.985	9.61	0.062	
¹²C¹⁶O	16–15	1841.35	2.48	0.03	standing waves
¹³C¹⁶O	9–18	991.329	2.43	0.030	
¹³C¹⁶O	10–9	1101.350	2.75	0.028	
²⁸Si¹⁶O	14–13	607.599	2.31	0.005	
²⁹Si¹⁶O	13–12	557.179	0.89	0.005	
²⁹Si¹⁶O	26–25	1112.833	0.74	0.028	low S/N, see Fig. 2
³⁰Si¹⁶O	26–25	1099.708	0.39	0.028	tentative, see Fig. 2
HCN	7–6	620.304	2.65	0.005	
HCN	13–12	1151.452	2.22	0.062	tentative, see Fig. 2
SO	$13_{14}-12_{13}$	560.178	0.20	0.005	
NH₃	1_0-0_1	572.498	4.93	0.005	
U		988.255	1.37	0.030	or at 1003.215 MHz

Notes. First column gives the molecular name, second column the transition, third column the frequency of the line, fourth column the integrated intensity, fifth column the noise, and last columns some comments (if necessary). One line is still unidentified, and is indicated with a "U" in the first column.

the available line lists and collisional rates can be found in Decin et al. (2010). The thermodynamical structure (see Fig. B.1) determined by Decin et al. (2010) was confirmed using the new HIFI observations (Sect. 3.2). Modelling the CO and H_2O lines provides insight into to the cooling/heating rates by transitions of these molecules (see also Decin et al. 2006, 2010). As can be seen in Fig. B.3, H_2O transitions provide the main cooling agent in the region up to $\sim 2 \times 10^{15}$ cm, while adiabatic cooling takes over for the region beyond $\sim 2 \times 10^{15}$ cm.

In the first instance, the molecular abundance stratifications derived by Decin et al. (2010) were assumed to model the ^{13}CO, ^{28}SiO, ^{29}SiO, ^{30}SiO, HCN, and SO lines (see full black lines in Fig. 2 and full lines in Fig. B.2). Using the new HIFI observations, the ^{13}CO and ^{28}SiO abundance fractions were refined in the inner envelope (see dashed black lines in Fig. 2 and dashed lines in Fig. B.2).

The radiative transfer modelling for water included the 45 lowest levels of the ground state and first vibrational state (i.e. the bending mode $\nu_2 = 1$ at 6.3 μm) for all isotopologs. Level energies, frequencies, and Einstein A coefficients were extracted from the HITRAN water line list (Rothman et al. 2009). The H_2O-H_2 collisional rates were taken from Faure et al. (2007). The effect of including excitation to the first excited vibrational state of the asymmetric stretching mode ($\nu_3 = 1$) was tested, and was found to be negligible (Decin et al. 2010).

A good agreement was found for the HCN(7–6) line proving that the inner abundance fraction [HCN/H$_{tot}$] is $\sim 2.2 \times 10^{-7}$. The ^{13}CO $J = 9-8$ and $J = 10-9$ lines are somewhat underpredicted assuming a $^{12}CO/^{13}CO$ ratio of 14 as obtained by Decin et al. (2010). Decreasing this ratio to 7 yields a better fit, but we
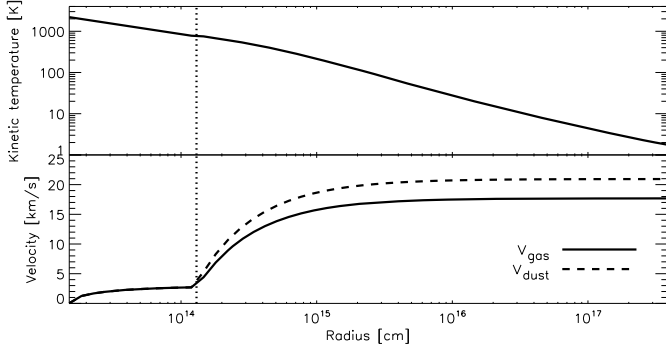
Fig. B.1. Thermodynamic structure of the envelope of IK Tau derived from the ^{12}CO $J = 1$–0 to $J = 7$–6 and HCN $J = 3$–2 and $J = 4$–3 rotational line transitions for the stellar parameters given in Table B.1 (Decin et al. 2010). The start of the dusty envelope, R_{inner}, is indicated by the dotted line.

Table B.1. (Circum)stellar parameters for IK Tau (Decin et al. 2010).

T_{eff} [K]	2200	[CO/H$_{tot}$]	1×10^{-4}
$R_\star$ [10^{13} cm]	1.5	^{12}CO/^{13}CO	14 (7)
$\dot{M}$ [$M_\odot$/yr]	8×10^{-6}	[^{28}SiO/H$_{tot}$]	8×10^{-6} (4×10^{-6})
distance [pc]	265	[^{29}SiO/H$_{tot}$]	3×10^{-7}
R_{inner} [$R_\star$]	8.7	[^{30}SiO/H$_{tot}$]	1×10^{-7}
v_∞ [km s^{-1}]	17.7	[HCN/H$_{tot}$]	2.2×10^{-7}
v_{turb} [km s^{-1}]	1.5	[SO/H$_{tot}$]	1×10^{-6} (1×10^{-5})
[ortho-H$_2^{16}$O/H$_{tot}$]	2.5×10^{-5}	OPR	3:1
H$_2^{16}$O/H$_2^{17}$O	600	H$_2^{16}$O/H$_2^{18}$O	200

Notes. T_{eff} is the effective stellar temperature, $R_\star$ denotes the stellar radius, $\dot{M}$ the gas mass-loss rate, R_{inner} the dust condensation radius, v_∞ the terminal velocity of the wind, and v_{turb} the turbulent velocity in the wind. The molecular fractional abundances are given relative to H$_{tot}$=n(H)+2n(H$_2$), and denote the abundance at the dust condensation radius (see Fig. B.2). Values between parentheses denote refined inner wind abundance values obtained from the new HIFI observations. The fractional abundances for all water isotopologs and isomers are based on the HIFI data presented in this Letter.

point out that the line profiles are quite noisy. The ^{13}CO fractional abundance was obtained assuming the same photodissociation radius as for ^{12}CO (Mamon et al. 1988). However, if the effect of less self-shielding of ^{13}CO (compared to ^{12}CO) were more important than estimated by Mamon et al. (1988), the photodissocation radius of ^{13}CO would be smaller, affecting the low excitation rotational transitions more than the higher excitation lines observed by HIFI. Another possibility might be that the velocity structure is steeper than the $\beta = 1$ power law now assumed in the region between ~20 and 150 $R_\star$, where these high-excitation lines are mainly formed. Since a constant mass-loss rate is assumed, this would imply a lower density in this region, and hence a higher ^{13}CO abundance fraction to produce the correct line intensity.

Only one higher-excitation ^{28}SiO line has been observed so far. The $J = 14$–13 transition indicates that the inner wind abundance might be a factor 2 lower than deduced by Decin et al. (2010), yielding an inner wind abundance of 4×10^{-6}, decreasing to 2×10^{-7} around 180 $R_\star$. The isotopolog line of ^{29}SiO(13–12) is very well predicted for an inner abundace of 3×10^{-7}; the higher excitation $J = 26$–25 line of both ^{29}SiO and ^{30}SiO are consistent with the HIFI observations. This implies an isotopic ratio of ^{28}SiO/^{29}SiO of 13.

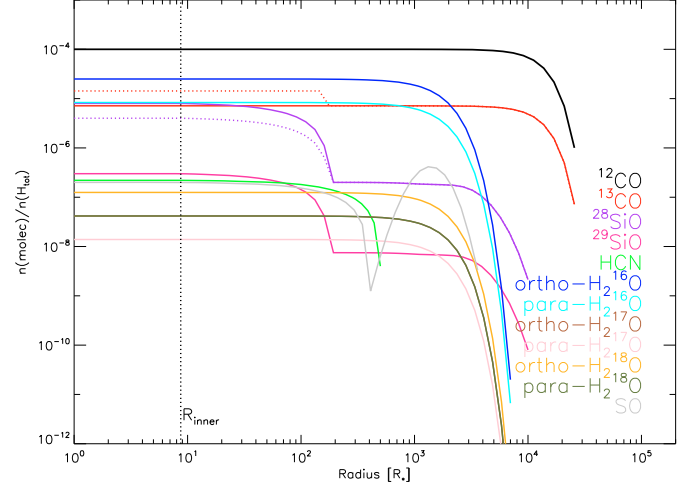Using the abundance pattern determined by Decin et al. (2010), the SO($13_{14} - 12_{13}$) is quite well predicted.

Fig. B.2. Fractional abundance stratifications for ^{12}CO, ^{13}CO, ^{28}SiO, ^{29}SiO, HCN, SO, ortho-H$_2^{16}$O, para-H$_2^{16}$O, ortho-H$_2^{17}$O, para-H$_2^{17}$O, ortho-H$_2^{18}$O, and para-H$_2^{18}$O. For all molecules (except water), the full line represents the results obtained by Decin et al. (2010). For ^{13}CO and ^{28}SiO, the new results based on the HIFI data are shown in dotted lines. The fractional abundances for all water isotopologs and isomers are based on the HIFI data presented in this Letter.
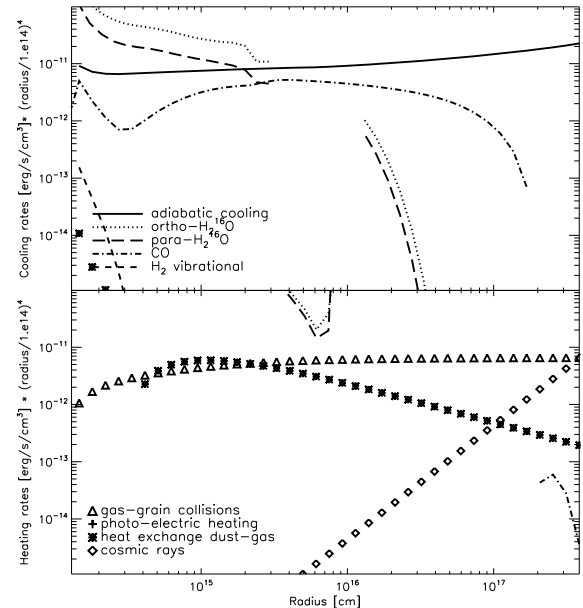

Fig. B.3. Cooling and heating rates in the envelope of IK Tau due to different processes (for details, see Decin et al. 2006). As can be seen in the plot, both CO and H$_2$O transitions mainly cool the envelope, but in certain restricted ranges can heat the envelope.